Oxygen Reduction by Lithiated Graphene and Graphene-Based Materials

Elmar Yu. Kataev,[†] Daniil M. Itkis,[*,†] Alexander V. Fedorov,[‡,∥,◆] Boris V. Senkovsky,[⊥,◆] Dmitry Yu. Usachov,[◆] Nikolay I. Verbitskiy,[†,‡,§] Alexander Grüneis,[‡] Alexei Barinov,[#] Daria Yu. Tsukanova,[†] Andrey A. Volykhov,[†,▽] Kirill V. Mironovich,[†] Victor A. Krivchenko,[†] Maksim G. Rybin,[○] Elena D. Obraztsova,[○] Clemens Laubschat,[⊥] Denis V. Vyalikh,[⊥,◆] and Lada V. Yashina[†]

[†]Moscow State University, 119991 Moscow, Russia, [‡]Universität zu Köln, Zülpicher Strasse 77, 50937 Köln, Germany, [§]Faculty of Physics, University of Vienna, Strudlhofgasse 4, A-1090 Vienna, Austria, [∥]IFW Dresden, P.O. Box 270116, D-01171 Dresden, Germany, [⊥]Institut für Festkörperphysik, TU Dresden, Mommsenstrasse 13, D-01069 Dresden, Germany, [#]Sincrotrone Trieste S.C.p.A., Area Science Park, I-34012 Basovizza, Trieste, Italy, [▽]Kurnakov Institute of General and Inorganic Chemistry RAS, Leninsky Av. 31, 119991 Moscow, Russia, [○]Prokhorov General Physics Institute, Russian Academy of Sciences, 119991, Moscow, Russia, and [◆]Department of Physics, St. Petersburg State University, 198504 St. Petersburg, Russia

ABSTRACT Oxygen reduction reaction (ORR) plays a key role in lithium–air batteries (LABs) that attract great attention thanks to their high theoretical specific energy several times exceeding that of lithium-ion batteries. Because of their high surface area, high electric conductivity, and low specific weight, various carbons are often materials of choice for applications as the LAB cathode. Unfortunately, the possibility of practical application of such batteries is still under question as the sustainable operation of LABs with carbon cathodes is not demonstrated yet and the cyclability is quite poor, which is usually associated with oxygen reduced species side reactions. However, the mechanisms of carbon reactivity toward these species are still unclear. Here, we report a direct *in situ* X-ray photoelectron spectroscopy study of oxygen reduction by lithiated graphene and graphene-based materials. Although lithium peroxide (Li_2O_2) and lithium oxide (Li_2O) reactions with carbon are thermodynamically favorable, neither of them was found to react even at elevated temperatures. As lithium superoxide is not stable at room temperature, potassium superoxide (KO_2) prepared *in situ* was used instead to test the reactivity of graphene with superoxide species. In contrast to Li_2O_2 and Li_2O, KO_2 was demonstrated to be strongly reactive.

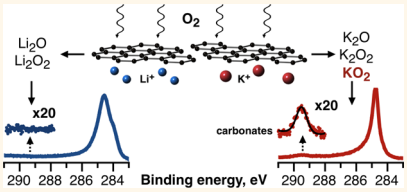

KEYWORDS: oxygen reduction reaction · graphene · carbon nanowalls · lithium–air battery · graphite intercalation compounds

Oxygen reduction reactions are involved in various important energy-related processes ranging from cell respiration in living organisms to electric power production in fuel cells and metal–air batteries. In electrochemical systems ORR occurs at electrocatalytic cathodes and is comprehensively studied in aqueous electrolytes.[1−4] ORR in nonaqueous media is much less investigated, and the lack of knowledge of ORR pathways and kinetics in aprotic solvents hinders the research and development of some new electrochemical devices, *e.g.*, nonaqueous lithium–air batteries capable to deliver specific energies as high as 900–1000 Wh/kg at the cell level according to theoretical estimations.[5] Such power sources use metallic lithium to reduce oxygen with the formation of a solid discharge product. At the first stage, oxygen is being reduced to a superoxide radical that can further undergo disproportionation in the presence of Li^+ ions[6] or receive another electron, finally forming lithium peroxide (Li_2O_2) in both cases (Figure 1a).

The sustainable operation of lithium–air batteries is still not reliably demonstrated due to lots of obstacles, including lithium dendrite growth at the negative electrode, side reactions of the electrolytes, and positive electrode degradation.[7] Most Li–air batteries reported in the literature utilize carbon as the positive electrode. Carbon materials are attractive due to their low cost, lightweight, high conductivity, and catalytic properties; unfortunately, they were recently demonstrated to be chemically unstable under the lithium–air battery operating conditions.[8−10] Such instability was suggested to arise from possible carbon reactivity toward discharge products,[8] intermediate species on discharge[10] or recharge.[11] These side reactions were found to lead to carbonate byproducts formation that, in turn, passivates and degrades the carbon electrodes, thus limiting rechargeability.

* Address correspondence to daniil.itkis@gmail.com.

Received for review September 15, 2014 and accepted January 5, 2015.

Published online January 05, 2015
10.1021/nn5052103

© 2015 American Chemical Society

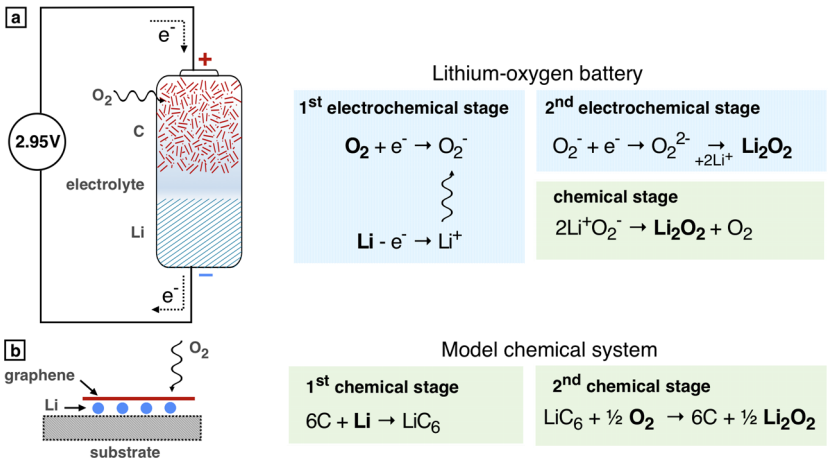

Figure 1. (a) Simplified scheme of the Li−oxygen battery and reactions occurring at the electrodes on discharge. (b) Model system for the study of oxygen reduction reactions suggested in this work. Lithium penetrates under the graphene layer after deposition, returning back to the surface when oxygen is supplied.

Investigations of oxygen reduction and side processes involving reduced species in electrochemical cells provide a complex picture composed of many chemical reactions with different cathode and electrolyte components. To overcome this issue, a few approaches that allow probing the reactivity of different materials and electrolytes toward oxygen reduced species were suggested. Reactions of lithium peroxide and oxide with hydrocarbons and CO_2 in gaseous phase were tested recently by *in situ* XPS.[12,13] Some works utilize KO_2 as a superoxide radical source to test electrolytes,[14,15] electrode binders,[15] or electrode materials.[10]

Here, we report a direct *in situ* XPS study of oxygen reduction by lithiated graphene and graphene-based materials and associated processes. We first employ angle resolved photoemission spectroscopy (ARPES) to characterize the evolution of electronic properties and electron transfer in the reactions of gaseous molecular oxygen with an idealized object—lithiated single layer epitaxial graphene (SLG), grown on Ni(111) substrates (Figure 1b). Next, we investigate lithium intercalation, followed by reactions of oxygen with multilayer graphitic materials: multilayer graphene (MLG) on Ni foil and free-standing carbon nanowalls (CNWs) on Si substrate, which both provide the possibility of the Li intercalation between graphene layers. We found that, for all the above-mentioned cases, reactions with oxygen lead to the formation of Li_2O_2 and Li_2O, while no evidence of further interaction of Li_2O_2 and/or Li_2O with the clean graphene surface was observed up to 500 °C. On the contrary, the epitaxial graphene was found to quickly react with potassium superoxide (KO_2) formed after oxygen exposure of KC_8 on the Ni(111) substrate. Carbonates were revealed as a final product of this reaction.

RESULTS AND DISCUSSION

Graphene grown on a Ni(111) substrate demonstrates a sharp LEED pattern (Figure S1, Supporting Information) and C 1s core-level photoemission spectrum shown in Figure 2a, which is typical for graphene grown on a Ni(111) substrate. The C 1s peak is shifted to lower binding energies in comparison to those for freestanding graphene samples due to its interaction with the substrate. The electronic band structure of graphene/Ni(111) along the ΓKM high symmetry direction in reciprocal space is exhibited in Figure 2b. Graphene on Ni(111) is strongly coupled to the substrate because of C $2p_z$ and Ni 3d hybridization.[16] Charge transfer and strong hybridization with Ni 3d states results in the graphene π-band being pushed down by 3 eV. The conical dispersion is destroyed near the Fermi level.[17]

Lithium deposition leads to ionization of lithium atoms, followed by transfer of 2s electrons to graphene. After the deposition and subsequent annealing at 150 °C, the C $2p_z$ and Ni 3d hybridization vanishes; therefore, the graphene π-band becomes shifted to the lower binding energies, and the partially filled π^*-band appears just below the Fermi level (Figure 2c).[18] Ni 3d states are not visible anymore, and linear band dispersion at the *K* point is clearly seen. Li intercalates under graphene, and the Li 2s band is not observed, evidencing that Li fully donates its valence electron to graphene, thus filling the Dirac cone up to ~1.6 eV above the Dirac point (detailed scan in the vicinity of the *K* point is plotted in Figure 2f). The C 1s peak is shifted to higher binding energies by 0.2 eV upon lithium deposition (Figure 2a). This value is lower than the typical shift for graphite after its lithiation (0.7−0.8 eV for LiC_6)[19−21] due to interaction of the sp^2 carbon network with the Ni substrate in the initial graphene sheet. C 1s asymmetry and broadening are also smaller for lithiated graphene, which can be explained by lower Drude plasmon contribution.[22] Being no more bound to Ni and injected with additional electrons coming from Li, lithiated graphene gains strong reduction ability toward molecular oxygen.

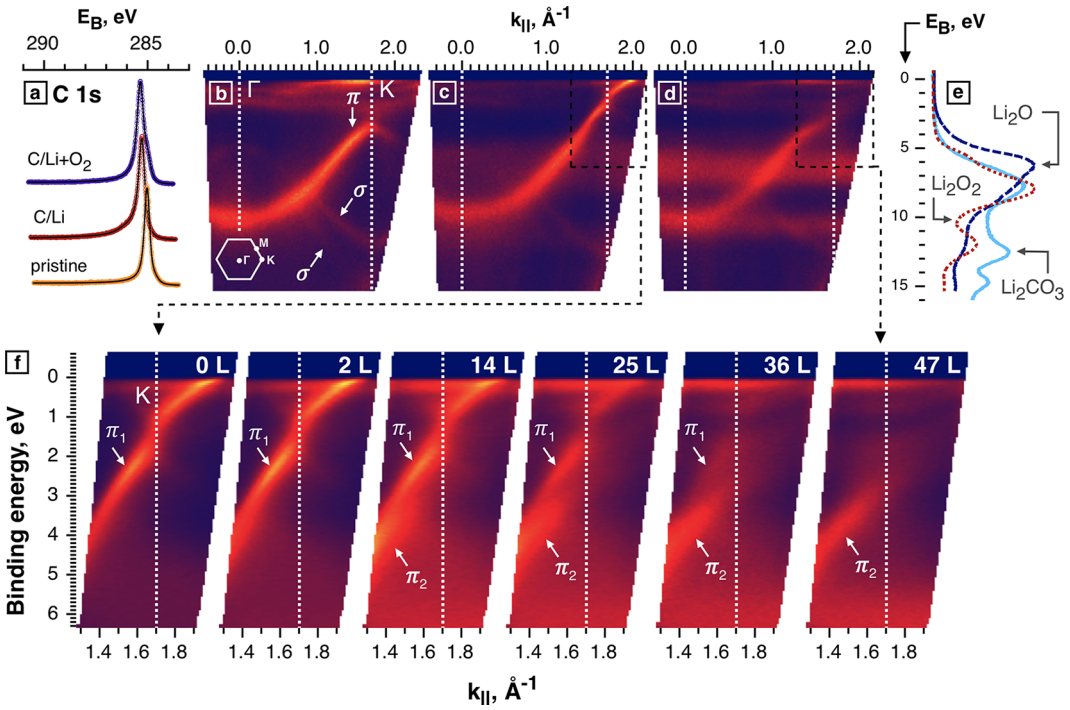

Figure 2. (a) C 1s photoemission spectra of pristine, lithiated, and oxygen exposed lithiated graphene. Experimental data are shown as colored circles; black lines represent fitting results. (b–d) ARPES of pristine (b), lithiated (c), and oxygen exposed (47 L) sample (d). (e) The valence band spectrum of Li_2O_2 (red dotted line) was recorded for CNW sample exposed to 256 L of oxygen at 5×10^{-8} mbar. Its further annealing at 500 °C resulted in Li_2O with VB spectrum plotted as blue dotted line. Li_2CO_3 (cyan line) VB spectrum was recorded for the Li–O_2 cell, discharged *in situ* in our previous work.[10] Energy axes of ARPES maps in (b–d) and VB spectra in (e) are aligned and have the same scale. (f) Evolution of ARPES recorded in the vicinity of K-point for lithiated graphene during oxygen exposure (exposure doses are indicated for each scan).

Oxygen exposures of the samples resulted in further electron transfer from lithiated graphene to oxygen, which is finally trapped at the surface in Li_2O_2 and Li_2O compounds identified by characteristic features in O 1s spectra in Figure 3a. Interestingly, the oxygen reduction proceeds with no uniformity across the sample surface manifested by the coexistence of electron-doped graphene regions and areas where graphene has already transferred its electrons to LiO_x species. Instead of continuous upshifting of the Dirac point, the sequence of the ARPES patterns recorded during oxygen exposure and shown in Figure 2f reveals two well-resolved π-bands corresponding to doped and undoped graphene regions. The evolution of C 1s spectra in Figure 3b also demonstrates multicomponent behavior with shifted and nonshifted components changing their relative intensities upon oxygen reduction/graphene oxidation, evidencing that relatively large product clusters are formed and cause graphene electron density depletion in their surrounding. As far as graphene is being oxidized back, the ARPES pattern in Figure 2d reveals two nondispersing bands, which can be ascribed to randomly oriented Li_2O and Li_2O_2 particles covering the graphene surface. Although consideration of such particles as an individual epitaxial phase with well-defined order is not possible, these surface layers reveal band positions corresponding to those in valence band spectra of oxygen exposed multilayer lithiated graphitic samples (Figure 2e) discussed below.

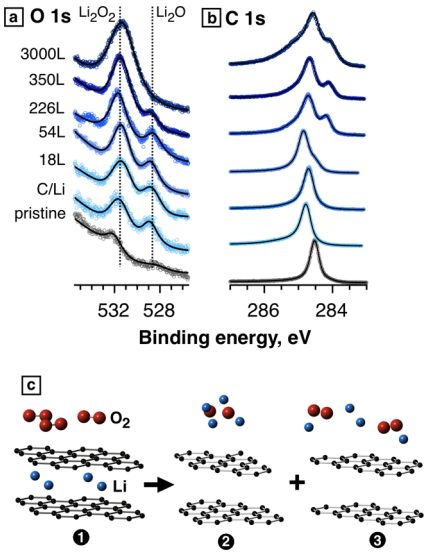

Figure 3. O 1s (a) and C 1s (b) photoemission spectra of pristine SLG, lithiated sample, and the same sample during oxygen exposure. (c) Minimal energy geometries for structures on bilayer graphene: (1) adsorbed oxygen on lithiated graphene, (2) lithium oxide cluster, (3) lithium peroxide cluster. Red, blue, and black spheres represent O, Li, and C atoms, respectively.

The stoichiometry of Li_2O and Li_2O_2 is further confirmed by O 1s (Figure 3a) and Li 1s (Figure S6, Supporting

TABLE 1. Summary of the Photoemission Spectral Features for Core Levels and Valence Band (VB)

	binding energy, eV										
	Li_2O_2			Li_2O			Li	Li_2CO_3			
reference	Li 1s	O 1s	VB	Li 1s	O 1s	VB	Li 1s	Li 1s	O 1s	C 1s	VB
this work	54.5	531.5	8, 11.5	53.5	528.5	6, 8					
24	56.6	534	8.5, 11.5	56.6	531.2	6	56	57.8	531.4	289.7	7, 15, 12
13	54.5	532		53.6	528.6			55.4	532	290	
25	56.4	533.1	11.3	55.6	530.6						
26		533	8.5		530	5.5					
27	55.6	531.5							532	290.5	
28	56.6	532.7		55	530.9					290.8	

Information) core-level spectroscopy. For that purpose, we had to additionally quantify the photoionization O 1s/Li 1s cross-section ratio for photoelectron kinetic energies below 200 eV as it cannot be properly calculated from the theoretical atomic subshell photoionization cross sections obtained with the Hartree−Fock−Slater one-electron central potential model for low kinetic energies[23] (Figure S8, Supporting Information). We believe that these data presented in the Supporting Information can be useful for composition quantification, *i.e.*, for those who investigate surface chemistry of lithium and oxygen containing compounds.

As Li_2O_2 and Li_2O were prepared *in situ* in submonolayer quantities, no contamination and charging effects were observed, in contrast to some *ex situ* experiments.[13,24,25] The binding energies of the O 1s level indicative for this system are estimated as 528.5 ± 0.1 and 531.5 ± 0.1 eV for oxide and peroxide, correspondingly. Li 1s, O 1s, and valence band component peak positions determined in our work are summarized in Table 1 together with previously reported data.[13,24−28] The experimental energy difference between Li_2O_2 and Li_2O O 1s spectra components of 2.5 ± 0.1 eV is in a reasonable correlation with the result of DFT calculations in the initial state approximation giving 2.8 and 3 eV differences for small clusters and for bulk phases, correspondingly (see Table 2).

As expected, the relative amount of Li_2O_2 grows upon oxygen exposure. In the lack of oxygen at low exposures, the surface layers have more lithium-rich Li_2O. This fact agrees with DFT calculations for small clusters on a graphene surface (Table 2), suggesting that oxide formation at the first stages is prevailing, while, at higher oxygen exposure doses, peroxide, which is more thermodynamically preferable in the bulk (see Table S1, Supporting Information), is being produced by the reaction $Li_2O + {}^1/_2O_2 = Li_2O_2$ (Figure 3a).

We further found that oxygen is being reduced *via* the same route by lithiated multilayer graphene-based materials, namely, multilayer graphene[29] and carbon nanowalls[30] both comprising up to 10−15 layers. In contrast to MLG, in which graphene layers are parallel

TABLE 2. DFT Calculated Formation Enthalpies (per Li Atom) and O 1s Chemical Shifts in Initial State Approximation[a]

structure	formation enthalpy, eV	O 1s chemical shift *vs* O_2, eV
(1) Oxygen physically adsorbed at lithiated graphene	−0.20	−0.4
(2) Li_2O on graphene surface	−2.01	−5.4
bulk Li_2O		−4.8
(3) Li_2O_2 on graphene surface	−1.80	−2.6
bulk Li_2O_2		−1.8

[a] Both chemical shifts and formation enthalpies are given relative to the $LiC_6 + O_2$ (at infinity) system (see Figure S8 for details).

to the substrate (Figure 4a), CNW represents freestanding multilayer graphene flakes that are oriented nearly vertically (Figure 4b; Figure S3, Supporting Information). For both lithiated CNW and MLG, oxygen exposure results in similar O 1s spectra evolution (Figure 4c). The Li_2O component detected at early stages is converted into a single Li_2O_2 component upon oxygen exposure. As the freestanding flakes in the CNW films have a random tilt, we were also able to record the angle integrated valence band photoemission spectra presented in Figure 4d and demonstrating reasonable agreement with the literature.[24] The valence band features for lithium oxide and peroxide are summarized in Table 1 and compared with ARPES data for these compounds formed at the surface of epitaxial graphene in Figure 2e.

Although CNWs have more edge atoms, which are often believed to be catalytically active,[31] the overall oxygen reduction rate was surprisingly found to be similar in the case of lithiated CNW and MLG samples. Conversion of oxygen to reduced oxygen species is plotted *vs* exposure dose in Figure 5a and shows no significant difference between the samples. In contrast, the lithium amount on the surface quantified as the Li:C ratio in Figure 5b significantly differs. Because of the much higher lithium diffusivity in the plane of graphite in comparison to that in the perpendicular direction (10^{-6} *vs* 10^{-11} cm^2/s),[32] lithium surface concentrations grow much faster in the CNW sample. In addition, from

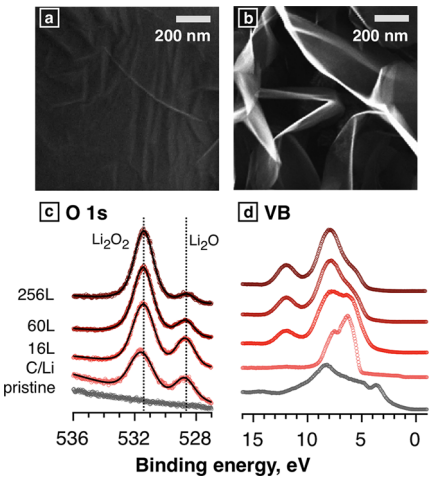

Figure 4. Top-view SEM images of the MLG (a) and CNW (b) samples. (c, d) O 1s and valence band photoemission spectra of pristine CNWs, lithiated CNWs, and the same sample during oxygen exposure.

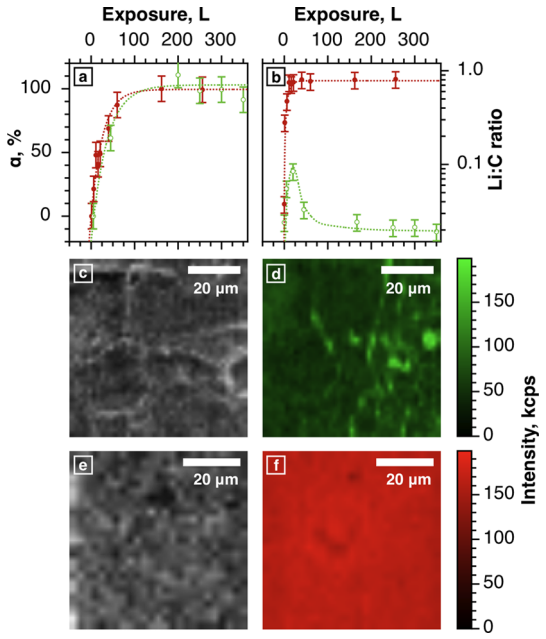

Figure 5. Oxygen to reduced oxygen species conversion (a) and Li:C ratio (b) *vs* oxygen exposure dose for lithiated MLG (green) and CNW (red). α was calculated as $\alpha = (I - I_{min})/(I_{max} - I_{min})$, where I, I_{min}, and I_{max} correspond to O 1s peak integral intensity at the current exposure point, at the beginning, and at the end of oxygen exposure, respectively. Dotted lines are shown for eye guidance. (c–f) Maps of the background signal intensity (c, e) associated with morphology and of the background-corrected Li 1s intensity (d, f), which represents reaction product distribution of oxygen exposed lithiated MLG (c, d) and CNW (e, f) samples.

spectromicroscopic data shown in Figure 5c–f, we found that, in micron scale, the coverage by reduction products is more uniform for carbon nanowalls than for multilayer graphene. In the latter case, lithium most probably goes to the surface *via* the defects and domain boundaries, thus leading to a formation of large product particles, nonuniformly distributed across the surface. As such particles can grow, leaving

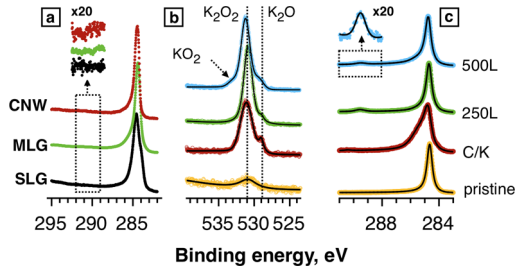

Figure 6. (a) C 1s photoemission spectra obtained after oxygen exposure of lithiated CNW (256 L, red points), MLG (320 L, green points), and SLG (350 L, black points) samples. (b–c) O 1s (b) and C 1s (c) photoemission spectra of pristine graphene, potassium intercalated sample, and the same sample during oxygen exposure. Experimental data are shown as circles; black curves represent the fitting results. Insets in (a) and (c) reveal the 292–288 eV range with fitted background subtracted and 20-fold increased intensity scale.

the carbon surface partially uncovered, we observe a maximum in Li:C ratio dependence on oxygen exposure.

In all materials under consideration (SLG, MLG, and CNW), lithium peroxide was identified as the final reduction product. In this study, we saw no evidence of its reactivity toward carbonaceous materials, although such a reaction is thermodynamically permitted for bulk substances (see Table S1 and work by McCloskey *et al.*).[8] DFT calculations on small clusters (Table S2, Supporting Information) yielded negative formation enthalpies as well; however, even a day-long observation of lithium peroxide on the surfaces of the materials under study did not reveal any carbonate signal in C 1s spectra (Figure 6a). As the CNW samples are expected to be the most reactive due to the large amount of defects (see Raman spectra in Figure S5, Supporting Information), we heated lithiated and oxygen exposed CNWs with Li_2O_2 formed on its surface up to 500 °C, but still no C 1s evolution was observed up to the Li_2O_2 thermal stability limit, which is estimated to be about 450 °C. At this temperature, thermal decomposition of lithium peroxide occurs ($Li_2O_2 = Li_2O + {}^1/_2O_2$) and lithium oxide is being formed (see O 1s and valence band spectra in Figure S11, Supporting Information). We have also probed the reactivity of lithium peroxide with carbon dioxide. Although Li_2O_2 is known as a CO_2 scavenging agent, we found that dry CO_2 does not react with lithium peroxide rapidly even at the surface, as most probably such a reaction can be strongly promoted by humidity.[33]

In contrast to oxygen exposure of lithiated graphene, in the case of the epitaxial graphene intercalated with potassium, carbonate is produced after treatment with oxygen. Along with the formation of oxide (K_2O) and peroxide (K_2O_2), oxygen exposure of potassium-intercalated graphene results in the generation of superoxide (KO_2) that is thermodynamically stable at room temperature and can be identified in O 1s spectra in Figure 6b.[26,34] At the same time, we detect

carbonate in the C 1s spectrum (Figure 6c). The carbon-to-carbonate conversion is estimated to be around 3%. Interestingly, that this value is roughly the same as the fraction of defects in the pristine graphene, grown at 600 °C (see Figure S2, Supporting Information). This finding leads us to a supposition that these are the oxygen-free imperfections in sp^2 carbon, which are responsible for the reactions with superoxide species. That agrees with our previous hypothesis on carbon reactivity toward superoxide intermediates produced in lithium–air batteries;[10] however, further detailed studies are required to find a reliable way toward stable electrode materials for oxygen reduction in aprotic media.

CONCLUSIONS

In conclusion, we have shown that oxygen reduction on the surface of lithiated graphene and graphene-based materials is accompanied by Li deintercalation and consequent lithium oxide and peroxide formation. We did not observe any reaction of graphitic carbons with peroxides and oxides produced *in situ*, while the appearance of superoxide species that were formed on potassium-intercalated graphene samples after oxygen exposure resulted in carbonate generation even for oxygen-free graphene. These findings reveal that it is the superoxide species that cause carbon-to-carbonate transformation, but it is still not completely clear what are the active sites in oxygen-free carbonaceous materials that are vulnerable to superoxide attacks. We believe that further investigation of graphene redox chemistry can shed light on this problem and facilitate the search for stable electrode materials for oxygen redox in aprotic media, thus enabling sustainable high-energy lithium–air batteries.

METHODS

Single layer graphene was prepared *in situ* under UHV conditions by CVD on Ni(111) single-crystalline film.[35] A 10 nm thick Ni film was grown epitaxially on a W(110) single crystal; then graphene was grown by exposure to 1×10^{-6} mbar of propylene (C_3H_6) at 590 or 600 °C for 5 min. Under these conditions, propylene decomposition reaction is self-limited to provide the formation of a single graphene layer. After each step of the preparation, sample quality was controlled using LEED.

The CNW films were grown *ex situ* in the DC glow discharge plasma in a mixture of hydrogen and methane, as described elsewhere.[30] Substrate temperature was held at 800 °C. The duration of the film deposition was 25 min. MLG samples were fabricated *ex situ* by CVD on nickel polycrystalline 25 μm thick foils according to a procedures described previously.[29] Synthesis was performed in two steps, including annealing of nickel foil and further film growth at 815 °C in a methane/hydrogen/argon mixture for 20 min. For cleaning, CNW and MLG films were annealed at 400 °C for 30 min and "flashed" three times at 550 °C for short periods of time to remove surface contaminations.

Lithium was deposited using the Li dispenser (SAES): 3 Å for SLG, 6 Å for MLG and CNW. The amount and deposition rate were controlled by a quartz microbalance and was set to 0.2 Å/min. After lithium deposition, samples were heated at 150 °C for 15 min to facilitate Li intercalation. Lithiated carbon samples were exposed to oxygen at 1×10^{-8} mbar.

ARPES experiments were performed using a photoelectron spectrometer equipped with a Scienta SES-200 hemispherical electron energy analyzer and a high flux He resonance lamp (Gammadata VUV-5010) in combination with a grating monochromator. All ARPES spectra were acquired at room temperature and a photon energy of 40.8 eV (He IIα), with an angular resolution of 0.2° and a total energy resolution of 50 meV. Electron band dispersions were measured along the Γ–*K*–*M* direction of the Brillouin zone by varying the polar-emission angle.

X-ray photoelectron spectroscopy (XPS) experiments were performed in Helmholtz Zentrum, Berlin, at RGBL beamline. Photoemission spectra were acquired using a SPECS Phoibos 150 electron energy analyzer at a base pressure better than 5×10^{-10} mbar. Total energy resolution was not worse than 0.1 eV. Photon energy was calibrated using second-order reflection of the diffraction from the plane grating. The energy scale of the electron analyzer was calibrated using the Au 4f line. The reproducibility of binding energy determination was estimated to be better than 0.05 eV. Spectra were fitted by Gaussian/Lorentzian convolution functions using a Unifit 2014 data processor. Asymmetry of the sp^2 component in C 1s core-level spectra was described with Doniach–Šunjić functions. Spectral background was optimized using a combination of Shirley and Tougaard functions simultaneously with spectral fitting. Atomic fractions were calculated from peak intensities obtained at fixed kinetic energy (more than 150 eV) normalized by photoionization cross sections and photon flux (see the Supporting Information for details).

The Li 1s photoemission and background intensity maps were acquired at Spectromicroscopy beamline of Elettra Sincrotrone in Trieste with 74 eV photon energy and 500 nm spatial resolution. The background was mapped using the integral intensity of signal in the 23.8–26.3 eV kinetic energy range. To obtain chemical contrast, the maps were recorded centering the kinetic energy window at 15 eV. The background intensity was then subtracted from the Li 1s intensity to obtain the Li 1s intensity lateral distribution.

DFT calculations were performed using a generalized gradient approximation (GGA) using the VASP package with projector augmented waves (PAW) functional to optimize the atomic structures. 5×5 *k*-points mesh of the first Brillouin zone and a $2\sqrt{3} \times 2\sqrt{3}$ supercell of the bilayered graphene were used for calculations. For the first approximation, we used clusters of minimal that allow maintaining a proper stoichiometry. All three calculated structures were isomeric. For the reference structure of $LiC_6 + O_2$ and for all other structures with excessive oxygen, oxygen in a form of an O_2 molecule was placed at infinity, *i.e.*, far enough from the graphene surface to avoid any interaction. The geometry was fully optimized. For comparison, we modeled bulk structures of Li_2O and Li_2O_2 using the same calculation conditions. The chemical shift in XP spectra for an atom of interest was calculated in initial state approximation as a variation of electrostatic potential taken in the center of the atom.[36]

Conflict of Interest: The authors declare no competing financial interest.

Supporting Information Available: Additional information about bulk thermodynamic properties, cross-section calculation, and detailed photoemission spectra. This material is available free of charge *via* the Internet at http://pubs.acs.org.

Acknowledgment. E.Y.K., L.V.Y., and D.Y.T. thank the Russian–German laboratory at HZB for financial support. The authors are grateful to HZB and ELETTRA for beamtimes granted. Research reported in this publication was supported by the Center for Electrochemical Energy of Skolkovo Institute of Science and Technology and BMBF (grant no. 05K120D3). V.A.K. and K.V.M. gratefully acknowledge the Russian president's young scientist support program (grant MK-2773.2014.2). The calculations were performed using SKIF and "Lomonosov" supercomputers of the Supercomputing Center of Lomonosov Moscow State University.

REFERENCES AND NOTES

1. Appleby, A. J. Electrocatalysis of Aqueous Dioxygen Reduction. *J. Electroanal. Chem.* **1993**, *357*, 117–179.
2. Chen, Z.; Higgins, D.; Yu, A.; Zhang, L.; Zhang, J. A Review on Non-Precious Metal Electrocatalysts for PEM Fuel Cells. *Energy Environ. Sci.* **2011**, *4*, 3167–3192.
3. Gasteiger, H. A.; Kocha, S. S.; Sompalli, B.; Wagner, F. T. Activity Benchmarks and Requirements for Pt, Pt-Alloy, and Non-Pt Oxygen Reduction Catalysts for PEMFCs. *Appl. Catal., B* **2005**, *56*, 9–35.
4. Suntivich, J.; Gasteiger, H. A.; Yabuuchi, N.; Nakanishi, H.; Goodenough, J. B.; Shao-Horn, Y. Design Principles for Oxygen-Reduction Activityon Perovskite Oxide Catalysts for Fuel Cells and Metal−Air Batteries. *Nat. Chem.* **2011**, *3*, 546–550.
5. Christensen, J.; Albertus, P.; Sánchez-Carrera, R. S.; Lohmann, T.; Kozinsky, B.; Liedtke, R.; Ahmed, J.; Kojic, A. A Critical Review of Li/Air Batteries. *J. Electrochem. Soc.* **2012**, *159*, R1.
6. Peng, Z.; Tarascon, J. M.; Freunberger, S. A.; Hardwick, L. J.; Chen, Y.; Giordani, V.; Bardé, F.; Novak, P.; Graham, D.; Bruce, P. G. Oxygen Reactions in a Non-Aqueous Li^+ Electrolyte. *Angew. Chem., Int. Ed.* **2011**, *50*, 6351–6355.
7. Lu, Y.-C.; Gallant, B. M.; Kwabi, D. G.; Harding, J. R.; Mitchell, R. R.; Whittingham, M. S.; Shao-Horn, Y. Lithium−Oxygen Batteries: Bridging Mechanistic Understanding and Battery Performance. *Energy Environ. Sci.* **2013**, *6*, 750–768.
8. McCloskey, B. D.; Speidel, A.; Scheffler, R.; Miller, D. C.; Viswanathan, V.; Hummelshøj, J. S.; Nørskov, J. K.; Luntz, A. C. Twin Problems of Interfacial Carbonate Formation in Nonaqueous Li−O_2 Batteries. *J. Phys. Chem. Lett.* **2012**, *3*, 997–1001.
9. Gallant, B. M.; Mitchell, R. R.; Kwabi, D. G.; Zhou, J.; Zuin, L.; Thompson, C. V.; Shao-Horn, Y. Chemical and Morphological Changes of Li−O_2 Battery Electrodes upon Cycling. *J. Phys. Chem. C* **2012**, *116*, 20800–20805.
10. Itkis, D. M.; Belova, A. I.; Semenenko, D. A.; Kataev, E. Y.; Neudachina, V. S.; Sirotina, A. P.; Hävecker, M.; Teschner, D.; Knop-Gericke, A.; Dudin, P.; *et al.* Reactivity of Carbon in Lithium-Oxygen Battery Positive Electrodes. *Nano Lett.* **2013**, *13*, 4697–4701.
11. Ottakam Thotiyl, M. M.; Freunberger, S. A.; Peng, Z.; Bruce, P. G. The Carbon Electrode in Nonaqueous Li−O_2 Cells. *J. Am. Chem. Soc.* **2013**, *135*, 494–500.
12. Lu, Y.-C.; Crumlin, E. J.; Carney, T. J.; Baggetto, L.; Veith, G. M.; Dudney, N. J.; Liu, Z.; Shao-Horn, Y. Influence of Hydrocarbon and CO_2 on the Reversibility of Li−O_2 Chemistry Using *In Situ* Ambient Pressure X-Ray Photoelectron Spectroscopy. *J. Phys. Chem. C* **2013**, *117*, 25948–25954.
13. Yao, K. P. C.; Quinlan, R. A.; Mansour, A. N.; Grimaud, A.; Lee, Y. L.; Lu, Y. C.; Shao-Horn, Y. Thermal Stability of Li_2O_2 and Li_2O for Li-Air Batteries: *In Situ* XRD and XPS Studies. *J. Electrochem. Soc.* **2013**, *160*, A824–A831.
14. Sharon, D.; Afri, M.; Noked, M.; Garsuch, A.; Frimer, A. A.; Aurbach, D. Oxidation of Dimethyl Sulfoxide Solutions by Electrochemical Reduction of Oxygen. *J. Phys. Chem. Lett.* **2013**, *4*, 3115–3119.
15. Black, R.; Oh, S. H.; Lee, J.-H.; Yim, T.; Adams, B.; Nazar, L. F. Screening for Superoxide Reactivity in Li-O_2 Batteries: Effect on Li_2O_2/LiOH Crystallization. *J. Am. Chem. Soc.* **2012**, *134*, 2902–2905.
16. Varykhalov, A.; Marchenko, D.; Sánchez-Barriga, J.; Scholz, M. R.; Verberck, B.; Trauzettel, B.; Wehling, T. O.; Carbone, C.; Rader, O. Intact Dirac Cones at Broken Sublattice Symmetry: Photoemission Study of Graphene on Ni and Co. *Phys. Rev. X* **2012**, *2*, 041017.
17. Grüneis, A.; Vyalikh, D. Tunable Hybridization Between Electronic States of Graphene and a Metal Surface. *Phys. Rev. B* **2008**, *77*, 193401.
18. Nagashima, A.; Tejima, N.; Oshima, C. Electronic States of the Pristine and Alkali-Metal-Intercalated Monolayer Graphite/Ni(111) Systems. *Phys. Rev. B* **1994**, *50*, 17487–17495.
19. Wertheim, G. K.; Van Attekum, P. T.; Basu, S. Electronic Structure of Lithium Graphite. *Solid State Commun.* **1980**, *33*, 1127–1130.
20. Lee, C. M.; Yang, S. H.; Mun, B. J.; Ross, P. N. Surface Structure of Lithiated Graphite by X-Ray Photoelectron Diffraction. *Surf. Sci.* **2001**, *477*, 126–132.
21. Mordkovich, V. Z. Synthesis and XPS Investigation of Superdense Lithium-Graphite Intercalation Compound, LiC_2. *Synth. Met.* **1996**, *80*, 243–247.
22. Liu, X.; Pichler, T.; Knupfer, M.; Fink, J. Electronic and Optical Properties of Alkali-Metal-Intercalated Single-Wall Carbon Nanotubes. *Phys. Rev. B* **2003**, *67*, 125403.
23. Yeh, J. J.; Lindau, I. Atomic Subshell Photoionization Cross Sections and Asymmetry Parameters: $1 \leqslant Z \leqslant 103$. *At. Data Nucl. Data Tables* **1985**, *32*, 1–155.
24. Ensling, D.; Thissen, A.; Jaegermann, W. On the Formation of Lithium Oxides and Carbonates on Li Metal Electrodes in Comparison to $LiCoO_2$ Surface Phases Investigated by Photoelectron Spectroscopy. *Appl. Surf. Sci.* **2008**, *255*, 2517–2523.
25. Wu, Q.-H.; Thissen, A.; Jaegermann, W. Photoelectron Spectroscopic Study of Li Oxides on Li Over-Deposited V_2O_5 Thin Film Surfaces. *Appl. Surf. Sci.* **2005**, *250*, 57–62.
26. Qiu, S. L.; Lin, C. L.; Chen, J.; Strongin, M. Photoemission Studies of the Interaction of Li and Solid Molecular Oxygen. *Phys. Rev. B* **1989**, *39*, 6194.
27. Dedryvère, R.; Martinez, H.; Leroy, S.; Lemordant, D.; Bonhomme, F.; Biensan, P.; Gonbeau, D. Surface Film Formation on Electrodes in a $LiCoO_2$/Graphite Cell: A Step by Step XPS Study. *J. Power Sources* **2007**, *174*, 462–468.
28. Töwe, M. Photoelectron Spectroscopy Studies of Carbon Based Fusion Reactor Materials. Ph.D. Thesis, University of Basel, Basel, Switzerland, 2003.
29. Obraztsov, A. N.; Obraztsova, E. A.; Tyurnina, A. V.; Zolotukhin, A. A. Chemical Vapor Deposition of Thin Graphite Films of Nanometer Thickness. *Carbon* **2007**, *45*, 2017–2021.
30. Krivchenko, V. A.; Dvorkin, V. V.; Dzbanovsky, N. N.; Timofeyev, M. A.; Stepanov, A. S.; Rakhimov, A. T.; Suetin, N. V.; Vilkov, O. Y.; Yashina, L. V. Evolution of Carbon Film Structure During Its Catalyst-Free Growth in the Plasma of Direct Current Glow Discharge. *Carbon* **2012**, *50*, 1477–1487.
31. Nakanishi, S.; Mizuno, F.; Abe, T.; Iba, H. Enhancing Effect of Carbon Surface in the Non-Aqueous Li-O_2 Battery Cathode. *Electrochemistry* **2012**, *80*, 783–786.
32. Persson, K.; Sethuraman, V. A.; Hardwick, L. J.; Hinuma, Y.; Meng, Y. S.; van der Ven, A.; Srinivasan, V.; Kostecki, R.; Ceder, G. Lithium Diffusion in Graphitic Carbon. *J. Phys. Chem. Lett.* **2010**, *1*, 1176–1180.
33. Selezneva, K. I. Interaction of Lithium Peroxide with Water Vapor and Carbon Dioxide. *Russ. J. Inorg. Chem.* **1960**, *5*, 820.
34. Lamontagne, B.; Semond, F.; Roy, D. K Overlayer Oxidation Studied by XPS: The Effects of the Adsorption and Oxidation Conditions. *Surf. Sci.* **1995**, *327*, 371–378.
35. Grüneis, A.; Kummer, K.; Vyalikh, D. V. Dynamics of Graphene Growth on a Metal Surface: A Time-Dependent Photoemission Study. *New J. Phys.* **2009**, *11*, 073050.
36. Yashina, L. V.; Zyubina, T. S.; Püttner, R.; Zyubin, A. S.; Shtanov, V. I.; Tikhonov, E. V. A Combined Photoelectron Spectroscopy and ab Initio Study of the Adsorbate System O_2/PbTe(001) and the Oxide Layer Growth Kinetics. *J. Phys. Chem. C* **2008**, *112*, 19995–20006.